Received: 7 September 2023 | Revised: 22 December 2023 | Accepted: 23 December 2023

DOI: 10.1002/htj.22999

ORIGINAL ARTICLE

HEAT TRANSFER WILEY

# Enhanced thermal performance and entropy generation analysis in a novel cavity design with circular cylinder

**Bijan Krishna Saha**[1] | **Jahidul Islam Jihan**[2] | **Md. Zobaer Ahammad**[1] | **Goutam Saha**[3,4] | **Suvash C. Saha**[4]

[1]Department of Mathematics, University of Barishal, Barishal, Bangladesh

[2]Department of Mechanical Engineering, Hajee Mohammad Danesh Science and Technology University, Dinajpur, Bangladesh

[3]Department of Mathematics, University of Dhaka, Dhaka, Bangladesh

[4]School of Mechanical and Mechatronic Engineering, University of Technology Sydney, Ultimo, New South Wales, Australia

**Correspondence**
Suvash C. Saha, School of Mechanical and Mechatronic Engineering, University of Technology Sydney, Ultimo, NSW 2007, Australia.
Email: Suvash.Saha@uts.edu.au

Goutam Saha, Department of Mathematics, University of Dhaka, Dhaka 1000, Bangladesh.
Email: gsahamath@du.ac.bd

**Abstract**

Analyzing fluid dynamics and heat transfer holds significant importance in the design and enhancement of engineering systems. The current investigation utilizes the finite element method to explore natural convection and heat transfer intricacies within a novel cavity containing an inner circular cylinder under steady and laminar flow conditions. The principal aim of this study is to assess the impact of Rayleigh number (*Ra*), Bejan number (*Be*), and the presence of adiabatic, hot, and cold cylinders on heat transfer, entropy generation, and fluid flow. The range of *Ra* considered in this investigation spans from $10^3$ to $10^6$, while the Prandtl number for the air is fixed at 0.71. The findings illustrate that the presence of a cylinder leads to higher *Be* as *Ra* increase, compared to scenarios where no cylinder is present. This observation suggests that buoyancy forces dominate in the absence of a cylinder, resulting in significantly enhanced convective heat transfer efficiency. However, the presence of a heated cylinder within the tooth-shaped cavity exerts a substantial influence on the overall thermal performance of the system. Notably, the average Nusselt

Number (*Nu*) experiences a remarkable increase of 41.97% under the influence of a heated cylinder, when compared to situations where a cold cylinder is present. This elevated average *Nu* signifies improved heat transfer characteristics, ultimately resulting in an overall improvement in the thermal system's efficiency.

**KEYWORDS**

cylinder, entropy generation, heat transfer, natural convection, tooth-shape cavity

## 1 | INTRODUCTION

In a plethora of engineering applications, many researchers delve into the examination of flow and heat transfer (HT) in a cavity. This phenomenon holds notable significance not only in nuclear reactors but also in various fields, including solar collectors, equipment cooling, thermal insulation, architectural design, aerosol systems, electrical systems, and numerous other technological processes.[1] The investigation of HT through natural convection (NC) remains an intriguing topic due to its correlation with diverse natural phenomena and industrial procedures. Ongoing inquiries persistently analyze the interaction between heat and fluid flow within cavities, with careful consideration of factors such as Rayleigh (*Ra*) and Prandtl (*Pr*) numbers, cavity geometry, and boundary conditions, given that these aspects can substantially influence the dynamics of HT.

The observation of buoyancy-driven flow is crucial in studying NC behaviors. Oliveski et al.[2] executed a numerical analysis to examine the characteristics of NC within a rectangular cavity to further explore this phenomenon. Yilbas et al.[3] witnessed a similar phenomenon within a square cavity. Through an extensive investigation, Chandra Roy et al.[4] discovered that factors including the angle of the magnetic field, heating, permeable walls, and nanoparticle concentration played pivotal roles in shaping both flow and temperature profiles, ultimately causing notable transformation. By conducting a numerical analysis, Momoniat et al.[5] found that the introduction of extended surfaces had a considerable effect on the distribution of temperature gradients, velocity streamlines, and flux within the square cavity. Furthermore, Akhter et al.[6] performed a computational investigation focusing on HT through NC in a partially heated cavity. The results demonstrated that buoyancy-driven flow exerted a substantial impact on the fluid flow and distribution of temperature within the cavity, along with the local entropy generation ($E_{gen}$). Kuyper et al.[7] examined the impacts of both laminar and turbulent flows on NC, concluding that the Nusselt number (*Nu*) demonstrates a significant correlation with *Ra*. Similarly, Kumar et al.[8] performed numerical simulation with a primary focus on NC within a square cavity. The findings revealed a direct correlation: as *Ra* went up, the results indicated a proportional growth in both the buoyancy-driven flow and the average HT. Mobedi[9] performed a numerical investigation focusing on NC within a square cavity. The study disclosed that as *Ra* rises and the conductivity ratio improves, there is an increased intensity in HT between the walls. The irregular shape of the cavity is another crucial factor that significantly influences the flow patterns and HT properties. Gaining a comprehensive understanding of the impacts of buoyancy-driven flow within irregular cavities holds paramount importance for various

applications, including HT in passive solar systems and building facades.[10] Chaabane et al.[11] conducted a numerical investigation to explore how buoyancy-driven flow is impacted by the irregular shape of a cavity. Thus, Hatami[12] conducted a thorough investigation into the NC HT of nanofluids within a rectangular cavity featuring two heated fins. The findings revealed that augmenting the fin height led to an expanded heated surface area, thereby increasing HT to the nanofluids and subsequently resulting in higher average temperatures. Similarly, Yousaf and Usman[13] performed a numerical investigation of NC HT within a square cavity featuring sinusoidal roughness elements. The study revealed a notable 28% decrease on average HT when the sinusoidal roughness elements were positioned simultaneously on both the hot and cold walls. Sheremet et al.[14] examined a numerical analysis of $E_{gen}$ during NC in a wavy cavity. The study revealed that an elevated *Ra* not only increased HT but also intensified the central convective flow and induced alterations in the recirculation patterns within the cavity. Saha et al.[15] performed a numerical study on NC flow of nanofluids within a wavy cavity. In this study, a heated single fin was vertically mounted at the center of the lower wall, adjacent to a top wavy wall. The study demonstrated that the presence of a wavy wall significantly enhances overall HT, leading to improved thermal performance. Siavashi et al.[16] researched delves into NC within a cavity equipped with porous fins. The numerical findings suggest that incorporating porous fins with a high Darcy number (*Da*) enhances HT, whereas fins with a low *Da* may impede convection, resulting in a reduction of *Nu*.

Conversely, nonuniform heating (NH) offers several advantages compared to uniform heating (UH). It serves as a sophisticated and effective strategy for optimizing temperature distribution and heat management within the system. Basak et al.[17] investigated the impact of NH and UH applied to the bottom walls on HT rate and presents correlations between average *Nu* and *Ra* for convection-dominated regimes. Thus, Sen et al.[18] observed a noteworthy improvement in HT through the implementation of NH, outperforming the effectiveness seen with UH. Biswas et al.[19] investigated the merits of NH over UH in a porous cavity. The study revealed that NH substantially enhances convective HT rates, leading to significantly higher overall HT compared to UH. Additionally, Mullick et al.[20] conducted a numerical investigation of NC inside a square cavity. The observation revealed that NH results in a more efficient and uniform distribution of heat within the cavity. Similarly, Natarajan et al.[21] explored the impact of UH and NH on the bottom wall on NC flows within a trapezoidal cavity. The results suggest that NH of the bottom wall results in an increased HT rate at the center compared to UH. Moreover, the use of NH prevents the formation of passive heat sources and irregular temperature patterns, guaranteeing a consistent distribution of temperature.[22] However, the introduction of cylinders into a cavity, along with NH, disrupts flow patterns and alters isotherms, leading to variations in HT characteristics.[23] This presents potential benefits for optimizing HT processes in a range of diverse applications. In a study by Şenel,[24] the interplay between the positioning, orientation of cylinders, initial temperature distribution, and the rotational direction holds a considerable influence on the dynamic flow patterns and temperature distribution within the cavity. A different investigation conducted by Joe et al.[25] revealed that the thermal performance of a trapezoidal cavity was improved by implementing NH at a variable frequency. This had an influence on thermofluidic patterns and the corresponding heat transmission. Bilal et al.[26] investigated the thermophysical characteristics of a viscous substance in a triangular container containing a heated square cylinder, examining the impact of UH and NH on the lower walls, and found that NH of the base wall was more efficient, resulting in increased *Nu* and kinetic energy as *Ra* increased.

Furthermore, NC flow is notably influenced by the presence of a cylinder within a cavity.[27] Moderres et al.[28] examined the impact of a cylinder within a cavity on NC flow, revealing that the presence of the cylinder can alter the flow pattern and enhance heat and mass transfer.

Similarly, Saleh et al.[29] examined NC within a porous cavity featuring a temperature gradient between an outer cavity and an inner cylinder. The study revealed that the circulation intensity of the flow is affected by the cylinder's radius, and an increased nanoparticles concentration leads to improved HT. On a related note, Tayebi et al.[30] conducted numerical simulations investigating $E_{gen}$ and NC in a square cavity filled with a hybrid nanofluid and featuring a conducting hollow cylinder. The outcomes underscore the pivotal role of the inserted conducting hollow cylinder in influencing flow characteristics, HT rates, and irreversibility's within the cavity. Similarly, Roslan et al.[31] numerically investigated to explore the intricacies of unsteady NC within a cavity featuring a sinusoidally heated cylindrical source. The insightful analysis uncovered that the oscillation in the cylinder's temperature exerts a profound influence on both the flow and temperature fields. Tayebi et al.[32] investigated convective heat transfer in a square container with a combination of nanofluid and a curved conductive cylinder, and discovered that the circulation of convective flow increases with higher Rayleigh number and lower Hartmann number. Alsabery et al.[33] investigated $E_{gen}$ and mixed convection (MC) in a wavy-walled chamber with a rotating cylinder. The study demonstrated that adjusting the rotational speed of the circular cylinder allows control over fluid flow. To further enhance the heat characteristics and flow behavior, Alsabery et al.[34] investigated another study of the impact of a two-phase nanofluid model on NC in a square cavity with a conducting solid block and a corner heater. The study revealed that *Nu* increases with higher nanoparticle concentrations and *Ra*, indicating an enhancement in HT. Conducting a numerical investigation, Alhashash et al.[35] explored NC of nanofluids between a sinusoidal cylinder and a rectangular cavity. The outcomes revealed that introducing 1% alumina particles can boost the HT rate. Dogonchi et al.[36] performed an NC and *Egen* of a nano-liquid in a crown-wavy cavity. It was found that *Da* had a positive effect on flow and temperature fields and increasing *Da* from 0.001 to 0.1 enhanced avg *Nu* by 41%. In a recent study conducted by Saboj et al.,[37] $E_{gen}$ was investigated within an octagonal cavity containing a cold cylinder. The findings revealed a notable increase in both HT and $E_{gen}$, particularly evident in the $Al_2O_3$–$H_2O$ nanofluid when compared to conventional fluids like air and water. Saleh et al.[38] studied on unsteady MC within a square cavity with fins. The results indicated that the movement direction of the attached fins has an impact on both the convective flow pattern and its intensity. Saha et al.[39] systematically reviewed HT analyses within cavities, aiming to comprehensively grasp flow and HT phenomena amidst diverse obstacles. The study underscored significant HT enhancement within cavities featuring elements such as fins and rotating cylinders. Some related research can be found in Ikram and colleagues.[40–45]

The aspiration of fluid in a cavity has significant effects on convection HT. It has been observed by Biswas et al.[46] that the implementation of aspiration can intensify HT in low-power MHD thermal applications. In a double lid-driven porous cavity, the aspiration of surrounding fluid results in heightened HT compared to a nonaspirated cavity, with enhancements of up to 180% depending on the specific parameters.[47] Conducting both experimental and numerical studies, Vishnu et al.[48] investigated the impact of HT on an open cavity exposed to supersonic crossflow. The observations revealed that the introduction of aspiration induces alterations in flow dynamics, including the expansion of the recirculation region and oscillation of the shear layer. The effectiveness of aspiration has been investigated in different arrangements, such as differential heating, corner heating, and split heating, and has demonstrated enhanced HT in all instances.[49]

Based on this brief discussion, it can be concluded that analyzing HT and $E_{gen}$ within an irregular geometry with an internal cylinder has been an intriguing phenomenon. What sets

our study apart is its primary focus on analyzing HT, $E_{gen}$, and *Be* within cavities that feature distinct cylinder boundary conditions with innovative geometric arrangements. While prior research has explored heat transfer phenomena in various cavity shapes, such as square and wavy topologies, there has been limited exploration of HT, $E_{gen}$, and *Be* within intricate geometries involving diverse cylinder boundary conditions. However, the tooth-shaped cavity introduces innovative HT traits, presenting promising prospects for application in thermal management systems. Here is one of the specific practical implications of Tooth shaped cavity. The tooth-shaped cavities are designed to fit together efficiently, maximizing the utilization of available space within the cold storage system. This design incorporates features aimed at minimizing heat transfer between items stored in different cavities, thereby ensuring a consistent temperature throughout the system and enhancing overall efficiency. To further optimize temperature control, the design promotes enhanced air circulation within the storage system, facilitating uniform cooling across all parts of the tooth-shaped cavities. This innovative approach not only maximizes space utilization but also contributes to maintaining a consistently low temperature for stored items.

## 2 | PHYSICAL MODEL

The physical model is developed to represent a tooth-shaped cavity with curved walls which is shown in Figure 1. Inside the cavity, a cylinder is introduced under various boundary conditions. The solid cylinder is located at the geometry's origin, as shown by the coordinate systems of $x$, $u$ and $y$, $v$. As it is marked in Figure 1, $L$ represents the longitudinal dimension, cylinder's radial measurement $r = .26$ L and the right and left curved halves of the walls are cooled to temperature $T_c$. The lower curved boundary is considered the hot wall $T_h$, while the upper wavy wall and the rest of the walls are kept adiabatic with no-slip conditions. The gravitational acceleration acts in a downward direction.

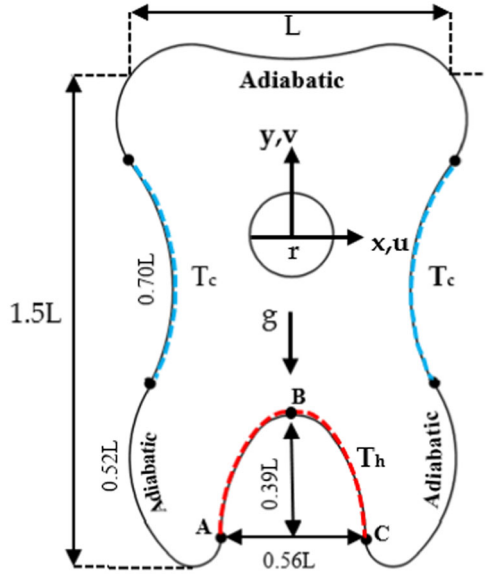


FIGURE 1 A visual representation of tooth-shaped cavity.

## 3 | MATHEMATICAL MODEL

The key equations that govern the considered problem incorporate the principles of conservation of mass, momentum, and energy in the fluid domain within the tooth-shaped cavity and heat conduction equations for the hot and cold walls. Our models assume Newtonian behavior and incompressible flow, showcasing steady and laminar flow through its mathematical representation. The effect of radiative heat transfer, viscous dissipation, and magnetic force are neglected in this study. The two-dimensional Navier–Stokes equations, which govern the fluid flow and the energy that governs the HT, are presented in a dimensional format, as below[39,50]:

$$\frac{\partial u}{\partial x} + \frac{\partial v}{\partial y} = 0, \tag{1a}$$

$$\rho\left(u\frac{\partial u}{\partial x} + v\frac{\partial u}{\partial y}\right) = -\frac{\partial p}{\partial x} + \mu\left(\frac{\partial^2 u}{\partial x^2} + \frac{\partial^2 u}{\partial y^2}\right), \tag{1b}$$

$$\rho\left(u\frac{\partial v}{\partial x} + v\frac{\partial v}{\partial y}\right) = -\frac{\partial p}{\partial y} + \mu\left(\frac{\partial^2 v}{\partial x^2} + \frac{\partial^2 v}{\partial y^2}\right) + \rho g\beta(T - T_0), \tag{1c}$$

$$\rho C_p\left(u\frac{\partial T}{\partial x} + v\frac{\partial T}{\partial y}\right) = \alpha\left(\frac{\partial^2 T}{\partial x^2} + \frac{\partial^2 T}{\partial y^2}\right). \tag{1d}$$

The governing Equations (1a)–(1d) are reduced to dimensionless form using the following dimensionless variables, together with the accompanying boundary conditions as follows:

$$X = \frac{x}{L}, Y = \frac{x}{L}, U = \frac{u}{\alpha L}, V = \frac{v}{\alpha L}, \theta = \frac{(T_f - T_c)}{(T_h - T_c)}. \tag{2}$$

The dimensionless stream function and vorticity are provided in the following manner,[51]

$$U = \frac{\partial \psi}{\partial \mathrm{Y}}, V = -\frac{\partial \psi}{\partial X} \text{ and } \frac{\partial V}{\partial X} - \frac{\partial U}{\partial Y} = \Omega. \tag{3}$$

The continuity equation inherently fulfills the mentioned stream function equation. Simultaneously, the vorticity equation is derived through the vorticity stream function method, which allows for the removal of the pressure term in the momentum equation. Hence, the governing equation in dimensionless form is presented below:

$$\frac{\partial^2 \psi}{\partial X^2} + \frac{\partial^2 \psi}{\partial Y^2} = -\Omega. \tag{4a}$$

$$U\frac{\partial \Omega}{\partial X} + V\frac{\partial \Omega}{\partial Y} = Pr\left(\frac{\partial^2 \Omega}{\partial X^2} + \frac{\partial^2 \Omega}{\partial Y^2}\right) + RaPr\frac{\partial \theta}{\partial X}, \tag{4b}$$

$$\left(U\frac{\partial\theta}{\partial X}+V\frac{\partial\theta}{\partial Y}\right)=\left(\frac{\partial^2\theta}{\partial X^2}+\frac{\partial^2\theta}{\partial Y^2}\right), \tag{4c}$$

where $U$, $V$, $\theta$, $X$, and $Y$ represents dimensionless variables.

The dimensionless quantities present in the governing equations include $Ra$ and $Pr$ defined as[50]:

$$Ra=\frac{g\beta(T_C-T_h)L^3}{\vartheta\alpha},\ \mathrm{Pr}=\frac{\mu}{\rho\alpha}. \tag{5}$$

*Boundary conditions*:

$$\begin{aligned}
&\text{For all walls: } U=V=0, \psi=0\\
&\qquad\text{Case-1 (No Cylinder)}\\
&\text{For left and right curved walls (point indicated):} && \theta=-0.5\\
&\text{For bottom curved wall (pointindicated):} && \theta=0.5\\
&\text{For top wavy wall:} && \frac{\partial\theta}{\partial n}=0\\
&\qquad\text{Case-2 (adiabatic cylinder)}\\
&\text{For left and right curved walls (point indicated):} && \theta=-0.5\\
&\text{For bottom curved wall (point indicated):} && \theta=0.5\\
&\text{For top wavy wall:} && \frac{\partial\theta}{\partial n}=0\\
&\text{For cylinder surfaces:} && \frac{\partial\theta}{\partial n}=0\\
&\qquad\text{Case-3 (cold cylinder)}\\
&\text{For left and right curved walls (point indicated):} && \theta=-0.5\\
&\text{For bottom curved wall(point indicated):} && \theta=0.5\\
&\text{For top wavy wall:} && \frac{\partial\theta}{\partial n}=0\\
&\text{For cylinder surfaces:} && \theta=-0.5\\
&\qquad\text{Case-4 (hot cylinder)}\\
&\text{For left and right curved walls (point indicated):} && \theta=-0.5\\
&\text{For bottom curved wall (point indicated):} && \theta=0.5\\
&\text{For top wavy wall:} && \frac{\partial\theta}{\partial n}=0\\
&\text{For cylinder surfaces:} && \theta=0.5
\end{aligned} \tag{6}$$

*Entropy generation*:

An examination of *Egen* is undertaken to evaluate the thermal efficiency of the system. Consequently, this study is utilized as a reference for assessing the thermal performance of the cavity. Thermal and viscous influences were accountable for $E_{gen}$, according to our investigation. The dimensionless form of the local $E_{gen}$, local $Be$ ($Be_l$), and total entropy ($E_{total}$) is represented as follows[52]:

$$E_{total}=\left[\left(\frac{\partial\theta}{\partial X}\right)^2+\left(\frac{\partial\theta}{\partial Y}\right)^2\right]+\varphi\left[2\left(\frac{\partial U}{\partial X}\right)^2+2\left(\frac{\partial V}{\partial Y}\right)^2+\left(\frac{\partial^2U}{\partial Y^2}+\frac{\partial^2V}{\partial X^2}\right)^2\right]. \tag{7}$$

Here, $\varphi$ denotes the irreversibility factor, which is equal to $10^{-4}$.
Local Bejan number ($Be_l$)[53]:

$$Be_l = \frac{\left(\frac{\partial\theta}{\partial X}\right)^2 + \left(\frac{\partial\theta}{\partial Y}\right)^2}{E_{total}}. \tag{8a}$$

The average entropy generation ($E_{avg}$)[37]:

$$E_{avg} = \frac{\iint E_{total}\, dX\ dY}{\iint dX\ dY}. \tag{8b}$$

The average Bejan number ($Be_{avg}$)[37]:

$$Be_{avg} = \frac{\int_A \int_A Be_l dXdY}{\int_A \int_A dXdY}. \tag{8c}$$

The average Nusselt number ($Nu_{avg}$) as[54,55]:

$$Nu_{avg} = \left[ -\int \frac{\partial\theta}{\partial Y}\bigg|_{AB} dX + \int \frac{\partial\theta}{\partial Y}\bigg|_{BC} dX \right]. \tag{8d}$$

## 4 | METHODOLOGY AND VALIDATION

The nondimensional governing Equations (4a)–(4c), with the boundary conditions (6), were numerically solved using COMSOL and finite element method. The fluid flow model prioritizes stability with the application of P2–P1 discretization and Galerkin least square approach. Likewise, linear discretization techniques are utilized for HT within the fluid model. The computational domain has been divided into triangular mesh elements (as shown in Figure 2) to discretize the various flow variables within the domain. Different grid sizes were utilized to compute $Nu_{avg}$ at $Pr = 0.71$ and $Ra = 10^6$ to confirm the mesh independence of the numerical solution. Across all analogous computational scenarios outlined in this research, the uniform grid GS-7 is introduced, and the outcomes are detailed in Table 1.

To ensure the credibility of our computational approach and validate the obtained results, we conducted a meticulous discrepancy between the streamline and isothermal profiles for incompressible flow conditions at $Ra$ values of $10^5$ and $10^6$ within the octagonal cavity, as shown in Figure 3. The outcomes qualitatively agree with the prior findings by Saboj et al.[37] and Saha et al.[55] To further substantiate the accuracy of our numerical simulations, we cross-referenced the entropy generation results with those presented in Ilis et al.,[50] which focused on square geometries.

Figure 4 provides a visual representation of the remarkable coherence between our current results, and the earlier research of Ilis et al.,[50] underscoring the dependability of our findings. Moreover, Figure 5 offers a comprehensive comparison of our simulation results with the previously reported outcomes. This alignment between our findings and the observations

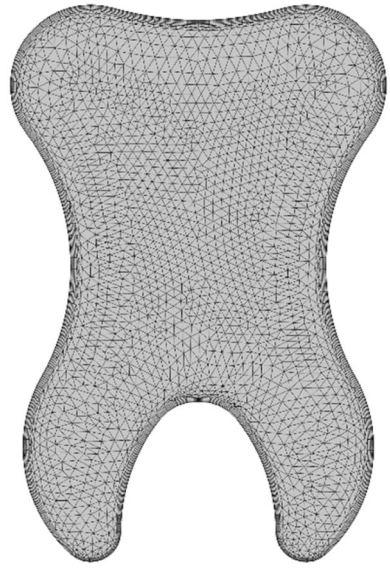

FIGURE 2 Triangular grid distribution containing 4860 elements.

TABLE 1 Variation of $Nu_{avg}$ with different grid-sizes.

| Grid size | Size of the elements | $Nu_{avg}$ |
|---|---|---|
| GS-1 | 4860 | 11.477 |
| GS-2 | 11,866 | 11.596 |
| GS-3 | 17,044 | 11.580 |
| GS-4 | 25,262 | 11.614 |
| GS-5 | 30,866 | 11.625 |
| GS-6 | 38,460 | 11.633 |
| **GS-7** | **43,626** | **11.642** |
| GS-8 | 49,812 | 11.644 |

outlined by Ilis et al.[50] enhances the overall trustworthiness and credibility of the conclusions drawn from our study.

## 5 | RESULTS AND DISCUSSION

### 5.1 | Streamline and isotherm profile variation (Case 1 and Case 2)

Figure 6 illustrates the streamlines and isotherms of the tooth-shaped cavity module under varying $Ra$ conditions, both with and without an inside cylinder. At $Ra = 10^3$, streamline profiles demonstrate two similar behaviors inside the cavity, regardless of the presence of an inside cylinder. Convection effects on the left and right cold walls impact the isotherm distribution differently when there is no cylinder module. When an inside cylinder is introduced, unique convection effects emerge due to interactions between the adiabatic

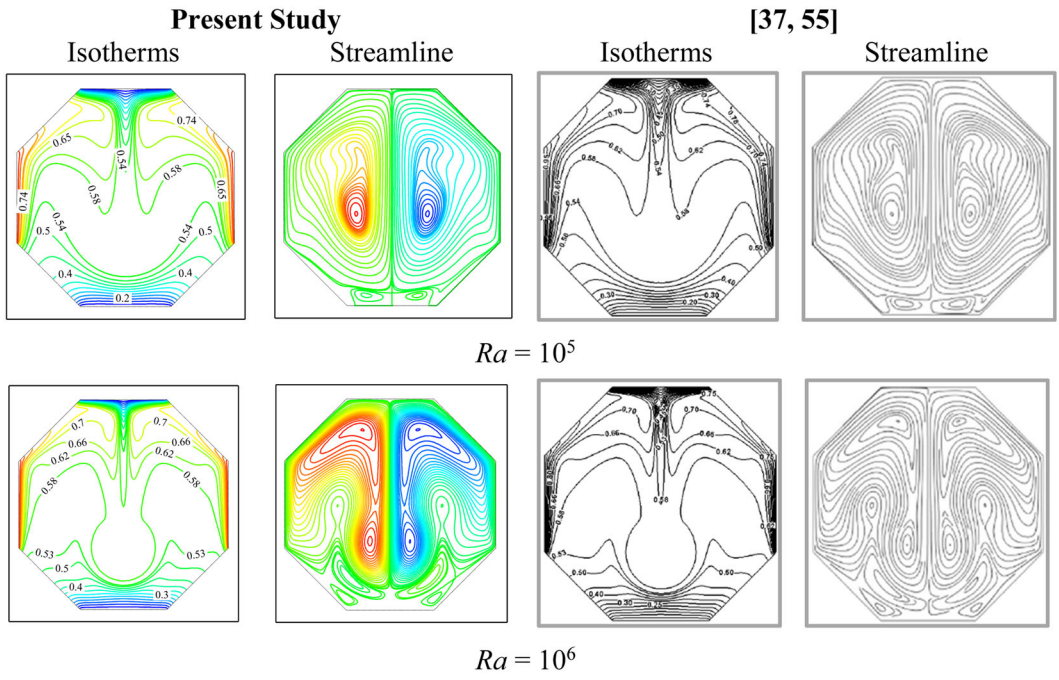


FIGURE 3 Comparison between the present isotherm and streamline profiles with results reported[37,55] at $Ra = 10^5$ and $Ra = 10^6$ with $Pr = 0.71$ for air.

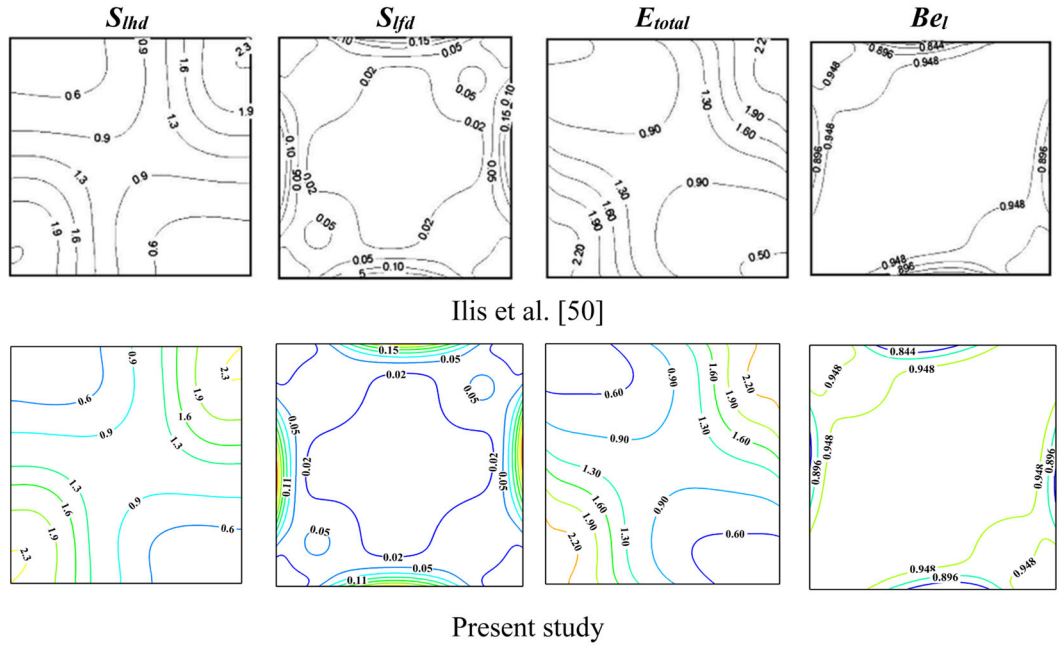


FIGURE 4 Comparative analysis of $S_{lhd}$, $S_{lfd}$, $E_{total}$, and $Be_l$ between Ilis et al.[50] and the present study at $Ra = 10^3$ and $AR = 1$.

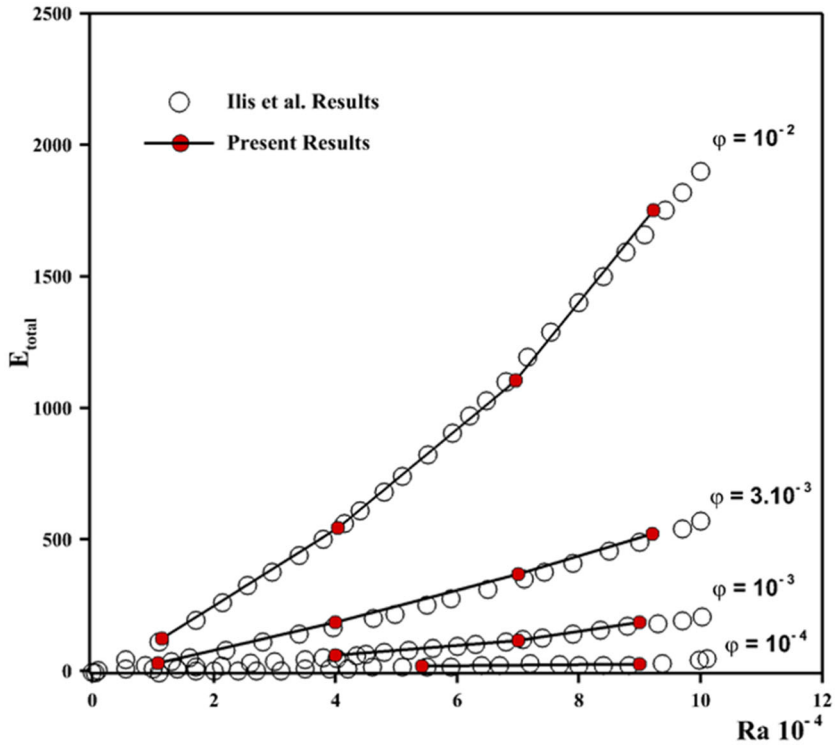


FIGURE 5 Comparison of previously published[50] numerical solutions with current results.

cylinder and the left, and right cold walls, leading to distinct alterations in the distribution of isotherms. The temperature distribution within the chamber is irregular and displays notable fluctuations at various positions in both scenarios. Moreover, the temperature difference between adjacent points within each region is minimal. Hence, a small temperature variation between nearby positions in different regions becomes noticeable. The isothermal profiles close to the two-sided cold boundary exhibit tightly distributed contours, whereas those at the top of the wavy adiabatic wall have flatter contours without cylinders. A similar trend can be seen when examining the inner cylinder module but with a distinction in the area near the adiabatic cylinder wall, where the contour is flatter. In the absence of cylindrical geometries, streamlines frequently demonstrate more uniform and consistent flow patterns compared to those observed within a cylindrical cavity. Additionally, as *Ra* increases, the buoyancy forces driving convection circulation become more potent, resulting in a significant distortion of the isothermal profile within the enclosed space.

Specifically, at $Ra = 10^4$, there is a substantial increase in flow intensity and this effect is subsequently magnified at *Ra* values of $10^5$ and $10^6$, respectively. At $Ra = 10^5$, streamlines begin to spread along the adiabatic upper wall, and this spreading increases further when $Ra = 10^6$. However, when placed inside a cylinder, the opposite effect occurs. As *Ra* increases, the streamlines spread toward the hot wall at the bottom. Increasing *Ra* results in stronger convection circulation leading to the isotherms becoming significantly more closely spaced near the two hot boundaries, the upper cold boundary and the cylinder, respectively. This is evident in the cases of $Ra = 10^5$ and $Ra = 10^6$. At higher *Ra* values, the isotherms become

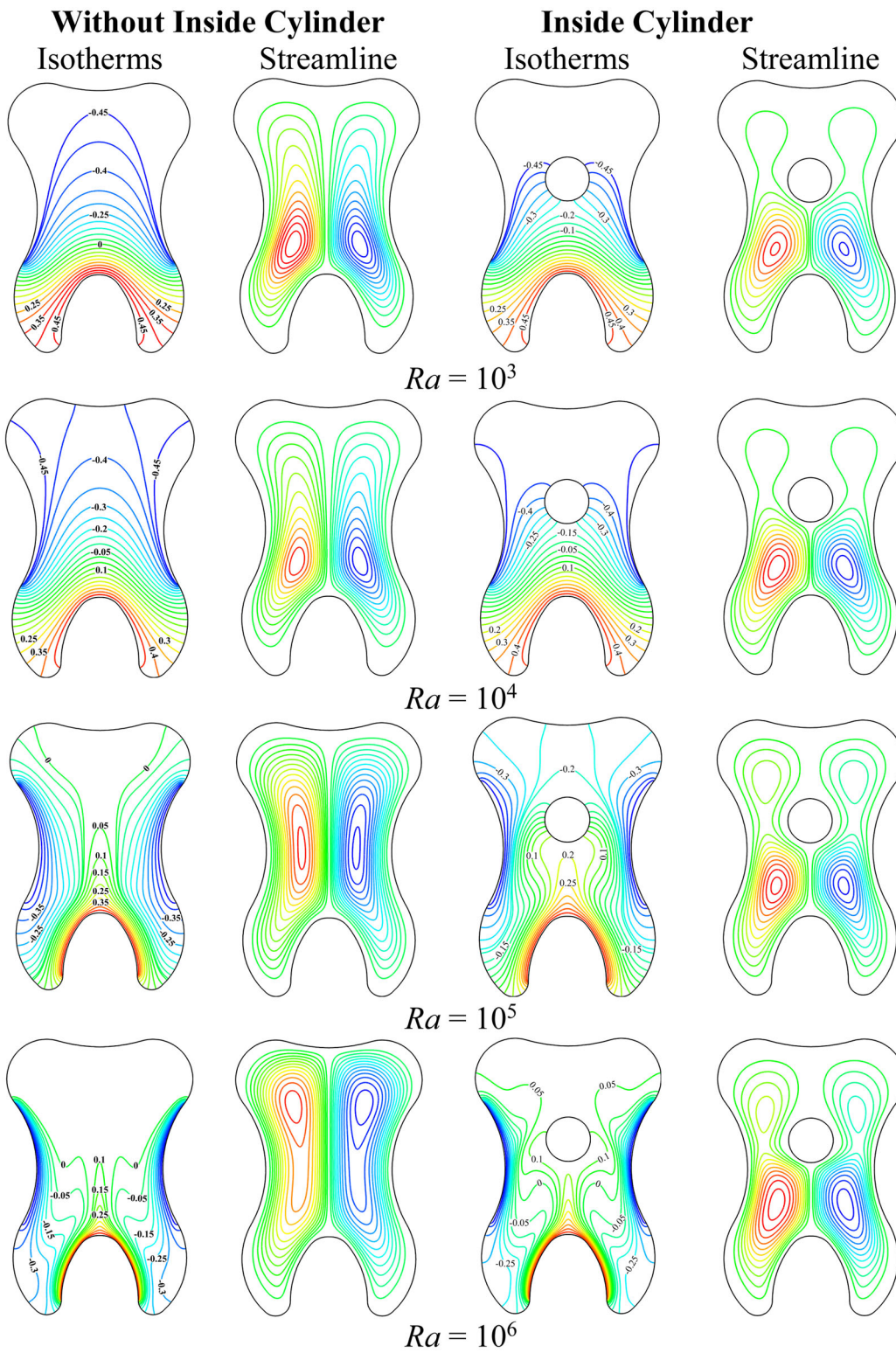


**FIGURE 6** Spatial distribution of streamline and isothermal profiles at $Ra = 10^3$, $Ra = 10^4$, $Ra = 10^5$, and $Ra = 10^6$, with a fixed $\varphi = 10^{-4}$, for with cylinder and without inside cylinder geometry.

denser and more closely spaced compared to lower values. With increasing *Ra*, convection circulation strengthens, resulting in closer spacing between isotherms near the heat walls of the bottom fin, the cold walls on the right and left, and in the case of cylinders, there are fewer contours, similar to $Ra = 10^5$ and $Ra = 10^6$.

## 5.2 | Variability in $E_{gen}$ (Case 1)

Figure 7 illustrates the contributions of $E_{gen}$ resulting from temperature difference and viscous dissipation, along with local $E_{gen}$ and $Be_l$, for *Ra* values ranging from $10^5$ to $10^6$ within without cylinder tooth-shaped cavity. At these elevated *Ra* values, convective effects play a dominant role in shaping fluid flow and determining $E_{gen}$. As a result, noticeable disparities in $E_{gen}$ become apparent between the scenarios of a domain without a cylinder and a domain with a cylinder, underscoring the significant impact of convection on the distribution of energy and entropy. In the case of a domain without a cylinder (Figure 7), it is evident that an increase in the value of *Ra* leads to a significant increase in the contours near the cold walls on the left and right, as well as the lower wall. However, when $E_{gen}$ due to HT dominates, there are no vortices

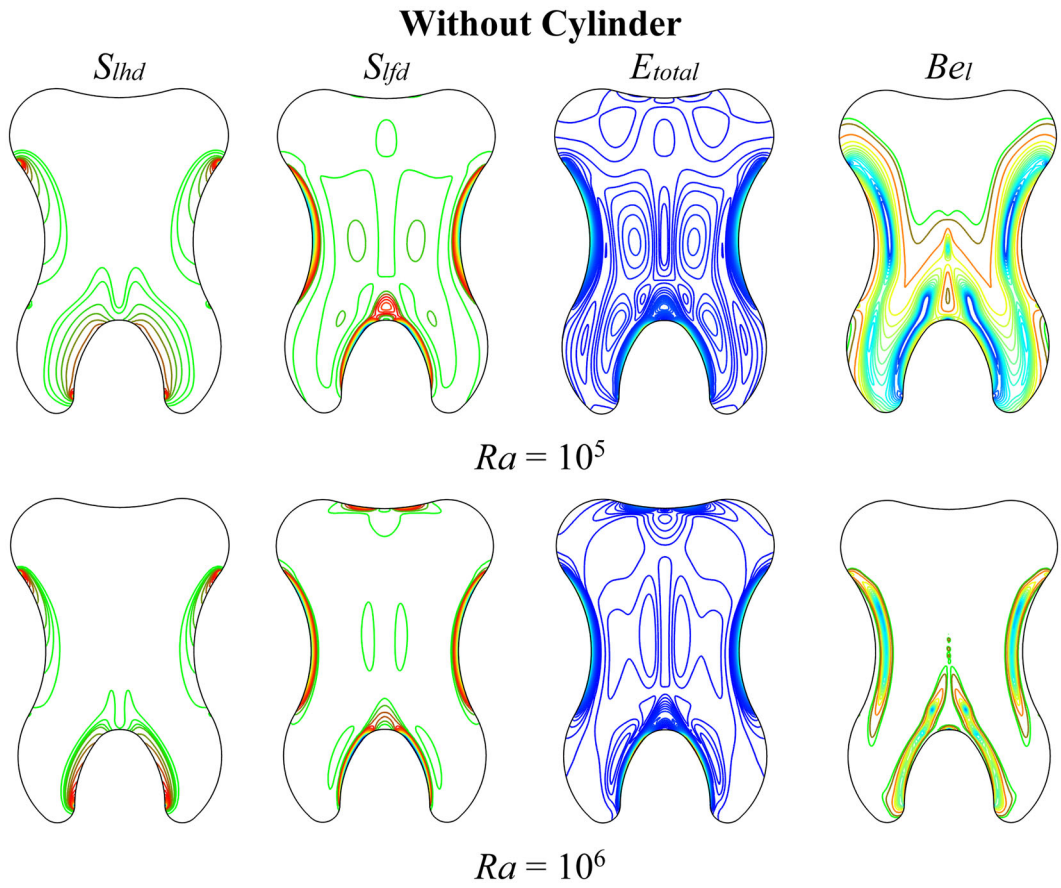


FIGURE 7 Spatial distribution of various $E_{gen}$ factors, including $S_{lhd}$, $S_{lfd}$, $E_{total}$, and $Be_l$ for $Ra = 10^5$ and $Ra = 10^6$ at $\varphi = 10^{-4}$ in the absence of cylinder geometry.

observed near the lower wall. As a consequence, HT occurs more uniformly in the vicinity of the bottom curved wall, contributing to reduced temperature fluctuations within the flow and resulting in a smoother, vortex-free motion near the lower boundary. Alternatively, when the value of $Ra$ is increased, a greater number of vortices emerge near the bottom wall, particularly when viscous dissipation exerts significant influence across the entire geometry. This phenomenon subsequently leads to an intensified HT rate near the lower boundary. Similar phenomena occur in the case of $E_{gen}$, where viscous dissipation is more dominant than HT. This leads to elevated local $E_{gen}$ contours near the walls. This phenomenon arises due to the enhanced viscous dissipation resulting from the smoother flow near the walls, which plays a significant role in contributing to $E_{gen}$. Similarly, the contours of $Be_l$ exhibit higher values near the wall boundaries where the elevated $Be_l$ suggests more efficient HT in those regions.

### 5.2.1 | Variability in $E_{gen}$ (Case 2)

Figure 8 illustrates the generation of $E_{gen}$ resulting from a temperature gradient and fluid friction, along with the representation of local $E_{gen}$ and $Be_l$ values for air within the range of $Ra = 10^5$ and $Ra = 10^6$, specifically focusing on the adiabatic inside cylinder. When dealing with

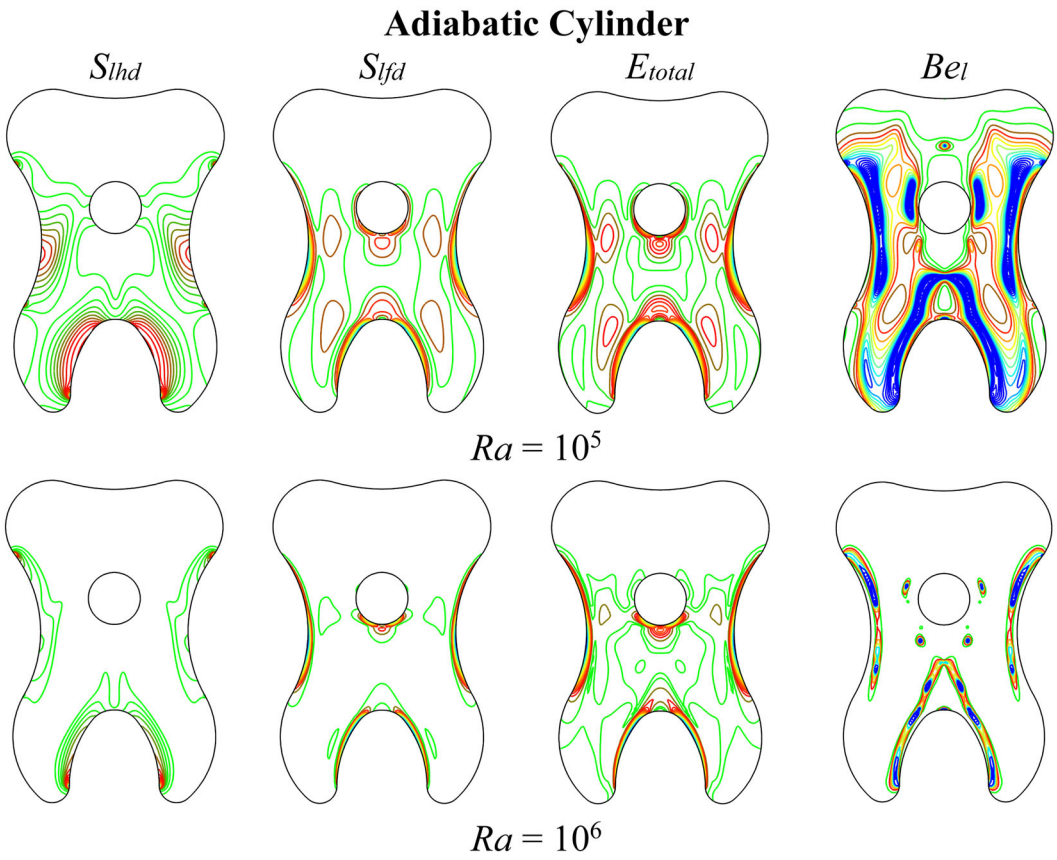


**FIGURE 8** Spatial distribution of various $E_{gen}$ factors, including $S_{lhd}$, $S_{lfd}$, $E_{total}$, and $Be_l$ for $Ra = 10^5$ and $Ra = 10^6$ at $\varphi = 10^{-4}$ in case of an adiabatic cylinder geometry.

a cylinder placed inside a tooth-shaped cavity, a significant *Ra* value leads to convective effects becoming predominant in influencing the fluid flow and the extent of $E_{gen}$. It can be observed in Figure 8 that increasing the value of *Ra* significantly enhances the contours near both the left and right cold walls, as well as the lower wall. When $E_{gen}$ due to HT is dominant, it can be seen that increasing the value of *Ra* results in nonuniform contours. This leads to a high variation of temperature throughout the geometry. Conversely, when the value of *Ra* increases, an increased number of vortices becomes apparent near the bottom wall and the cylinder wall. This phenomenon becomes particularly pronounced when viscous dissipation exerts significant dominance across the entire geometry, consequently leading to an enhanced HT rate near both the lower wall and the cylinder wall. Similarly, the average $E_{gen}$ decreases in comparison to the domain without a cylinder, primarily due to the heightened HT occurring at the lower wall, the cold side wall, and also as a result of the influence of the cylinder wall.

However, in the case of *Be*, HT decreases as the value of *Ra* increases, resulting in nonuniform contours towards the cylinder wall. Thus, the contour towards the cylinder wall is diminishing due to the dominance of HT, leading to an increase in the average value of *Be*. This results in an inefficient geometric model when compared to the boundary conditions without a cylinder.

Therefore, Table 2 demonstrates that for both cases—without a cylinder and with an adiabatic cylinder module—$Nu_{avg}$ increases while the *Ra* value increases, and there is a corresponding decrease in the *Be*. This correlation is expected, as higher *Ra* values signify more significant temperature disparities between the wall and fluid, leading to heightened HT rates. Additionally, it reveals that the average $E_{gen}$ increases as the *Ra* value escalates from $10^3$ to $10^6$, consistent with the earlier discussion. Moreover, Table 2 indicates that the utilization of a cylinder's presence inside the tooth cavity results in a lower average $E_{gen}$ under the same heating conditions. It also demonstrates that the average $E_{gen}$ is inversely related to *Ra* values: at lower *Ra* values, it is lower, whereas at higher *Ra* values, it becomes higher. When considering the *Be* values, it becomes evident that for both conditions at $Ra = 10^3$, *Be* exceeds 0.5. This observation suggests that $E_{gen}$ resulting from the temperature gradient holds greater influence than $E_{gen}$ due to fluid friction. Conversely, at *Ra* values ranging from $10^4$ to $10^6$, *Be* values drop below 0.5, signifying that $E_{gen}$ due to fluid friction becomes more prominent compared to $E_{gen}$ resulting from the temperature gradient. When considering the scenario without an inside cylinder, as *Ra* values progress from $10^3$ to $10^6$, the $Nu_{avg}$ value experiences a rise from 2.47 to 11.12, accompanied by an increase in the $E_{avg}$ value from 2.47 to 598.64. Concurrently, the *Be* value decreases from 0.99 to 0.025.

**TABLE 2** Variation of $Nu_{avg}$, $E_{avg}$, and *Be* of without cylinder and with adiabatic cylinder.

| Without cylinder | | | | With adiabatic cylinder | | | |
|---|---|---|---|---|---|---|---|
| ***Ra*** | $Nu_{avg}$ | $E_{avg}$ | ***Be*** | ***Ra*** | $Nu_{avg}$ | $E_{avg}$ | ***Be*** |
| $10^3$ | 2.47 | 2.49 | 0.99 | $10^3$ | 2.44 | 2.47 | 0.99 |
| $10^4$ | 2.52 | 2.68 | 0.81 | $10^4$ | 2.49 | 2.62 | 0.90 |
| $10^5$ | 5.40 | 33.11 | 0.16 | $10^5$ | 5.05 | 24.47 | 0.22 |
| $10^6$ | 11.64 | 675.78 | 0.025 | $10^6$ | 11.12 | 598.64 | 0.028 |

Likewise, when an inside adiabatic cylinder is introduced, the $Nu_{avg}$ value shows an increase from 2.44 to 11.64, accompanied by a notable increase in the value of $E_{avg}$ from 2.49 to 675.78. Simultaneously, the *Be* value experiences a decrease from 0.99 to 0.028 as *Ra* values increase from $10^3$ to $10^6$. When comparing the results between the scenarios of "without cylinder" and "with adiabatic cylinder," it becomes apparent that $Nu_{avg}$ is generally greater in the "without cylinder" scenario than in the "with adiabatic cylinder" scenario. This observation implies that HT is more effective in the case of the "without cylinder" scenario.

## 5.3 | Streamline and isotherm profile variation (Case 3 and Case 4)

Figure 9 illustrates the streamlines and isotherms of the tooth-shaped cavity module under different *Ra*, considering both cold cylinder and heated cylinder boundary conditions. For *Ra* values of $10^3$ and $10^4$, the streamline and isotherm profiles show similar contours under heated cylinder boundary conditions. These similarities arise from the distinct convection effects experienced by the bottom and cold walls of the cavity, as well as the heated cylinder. The temperature distribution within the cavity exhibits nonuniformity, indicating significant variations across different regions. Similarly, under cold boundary conditions, streamline and isotherm profiles display comparable contours. However, when the cylinder is cold, the highest temperature regions are concentrated in the lower half of the tooth-shaped cavity. In the case of a heated cylinder, it is noteworthy that the isotherms near the left and right cold walls and the heated cylinder have closely spaced contours, while those near the top wavy wall exhibit more evenly distributed contours. This arrangement results in stable convection and smoother, more regular flow patterns in the streamlines.

In contrast, when considering a cold cylinder, the temperature distribution becomes more linear, exhibiting reduced variation across distinct regions, and the maximum temperature is confined to the lower part of the cavity. Hence, the isothermal contours are closer together in the lower portion of the heated wall, and near the cold wall, they possess flatter contours. Recirculation also occurs in the lower portion of the tooth-shaped cavity, resulting in smoother flow patterns. As shown in Figure 9, an increase in *Ra* significantly impacts both isotherms and streamlines under both boundary conditions. When *Ra* increases, the buoyant force driving convection circulation becomes stronger, resulting in a clear distortion of the isotherm profiles within the cavity. Specifically, at $Ra = 10^5$, there is an expansion in the stream force, which is additionally enhanced at $Ra = 10^6$. Furthermore, at $Ra = 10^5$, streamlines are spreading downward in heated boundary conditions, which is more conspicuous at $Ra = 10^6$. However, it is worth emphasizing that despite these changes, the streamlines frequently exhibit smoother and more predictable patterns compared to those observed in the case of the cold cylinder. As *Ra* rises, the convective circulation intensifies, and the isotherms are forced to cluster closer to the heated cylinder wall, the two cold walls, and the lower hot wall.

On the other hand, in the case of a cold boundary condition, at $Ra = 10^5$, the streamlines also spread downwards, and the isotherms become tighter at the lower heated wall. At $Ra = 10^6$, the streamlines spread even more towards the lower wall, and a bubble forms on the side of the cold wall, leading to irregularities in the streamlines. Moreover, At $Ra = 10^6$, the isothermal contours become tight at the two cold side walls, the heated lower wall, and the cold cylinder wall due to the convection effect. However, the effect of convection HT is less pronounced compared to the heated cylinder boundary conditions.

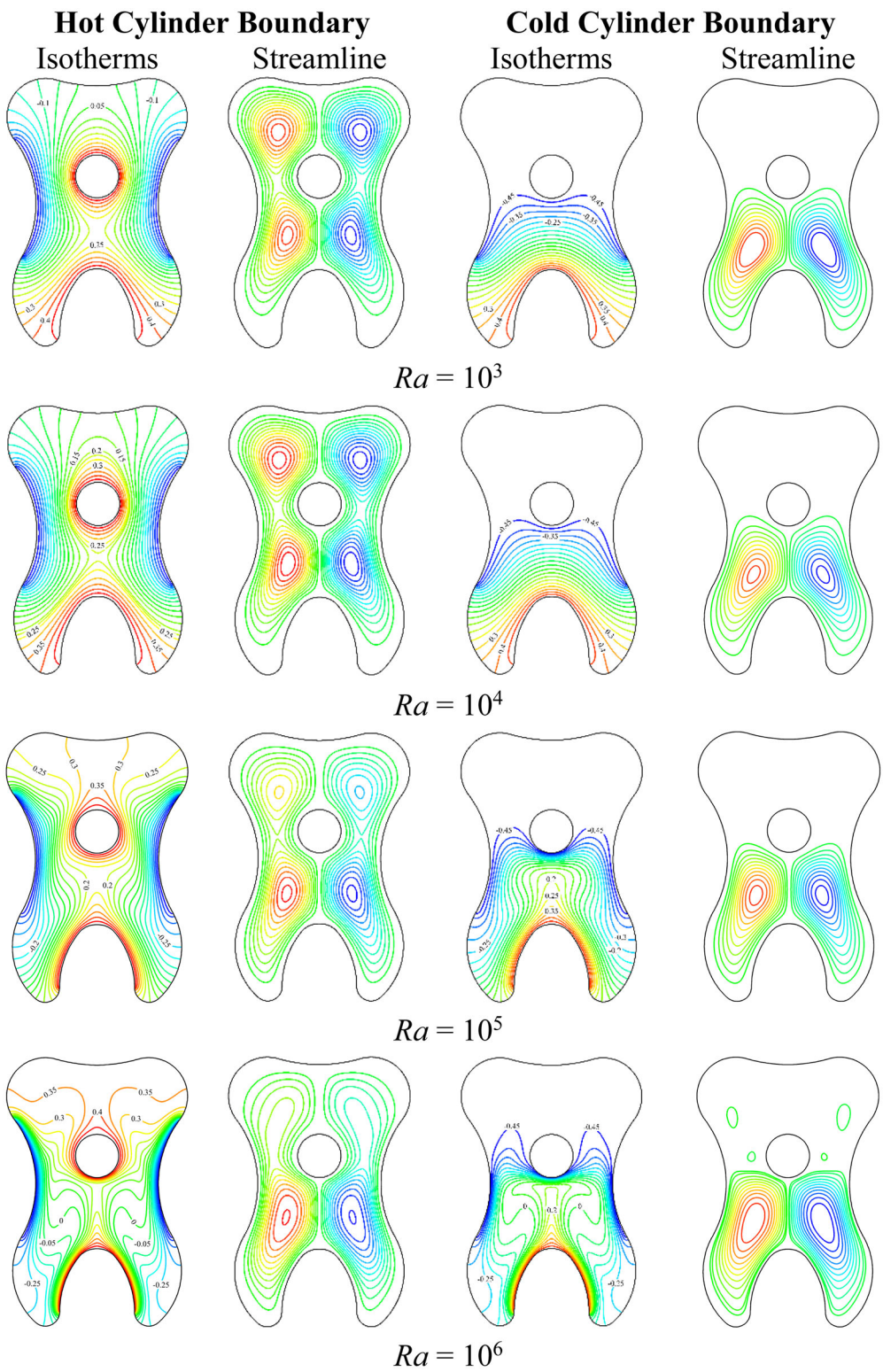


**FIGURE 9** Spatial distribution of streamline and isothermal profiles at $Ra = 10^3$, $Ra = 10^4$, $Ra = 10^5$, and $Ra = 10^6$, with a fixed $\varphi = 10^{-4}$ for cold and hot cylinder boundary conditions.

## 5.4 | Variability in entropy generation (Case 3)

For *Ra* values $10^5$ and $10^6$, the local $E_{gen}$ and local $Be_l$ are represented in Figure 10, together with the $E_{gen}$ induced by a temperature gradient and viscous dissipation. At this high *Ra*, convective processes begin to play a more significant role in regulating fluid movement and $E_{gen}$, resulting in considerable differences in $E_{gen}$ across domains with hot and cold cylinder boundary conditions. In the case of heated cylinder boundary conditions, it can be observed that increasing the value of *Ra* significantly increases the contour close to the left curve and right curve boundaries as well as the lower wall, whereas decreasing the contour near the heated cylinder when HT is dominant. However, in other cases, contours increase near the cold walls and heated walls when the value of *Ra* increases. There are no vortices near the lower and cylinder walls when $E_{gen}$ due to HT is dominant. Consequently, this leads to a more uniform heat transfer rate along the bottom and cylinder sides, resulting in reduced temperature fluctuations within the flow. This, in turn, contributes to a smoother flow pattern without any vortices forming at the bottom wall. On the other hand, by increasing the value of *Ra*, more vortices appear near the bottom and cylinder walls when viscous dissipation is significantly dominant in the entire geometry, which results in a greater HT rate near the lower wall. Similar things happen in the case of $E_{gen}$ due to the fact that viscous dissipation is more dominant compared to HT. This results in higher local $E_{gen}$ contours close to the walls. This arises from the fact

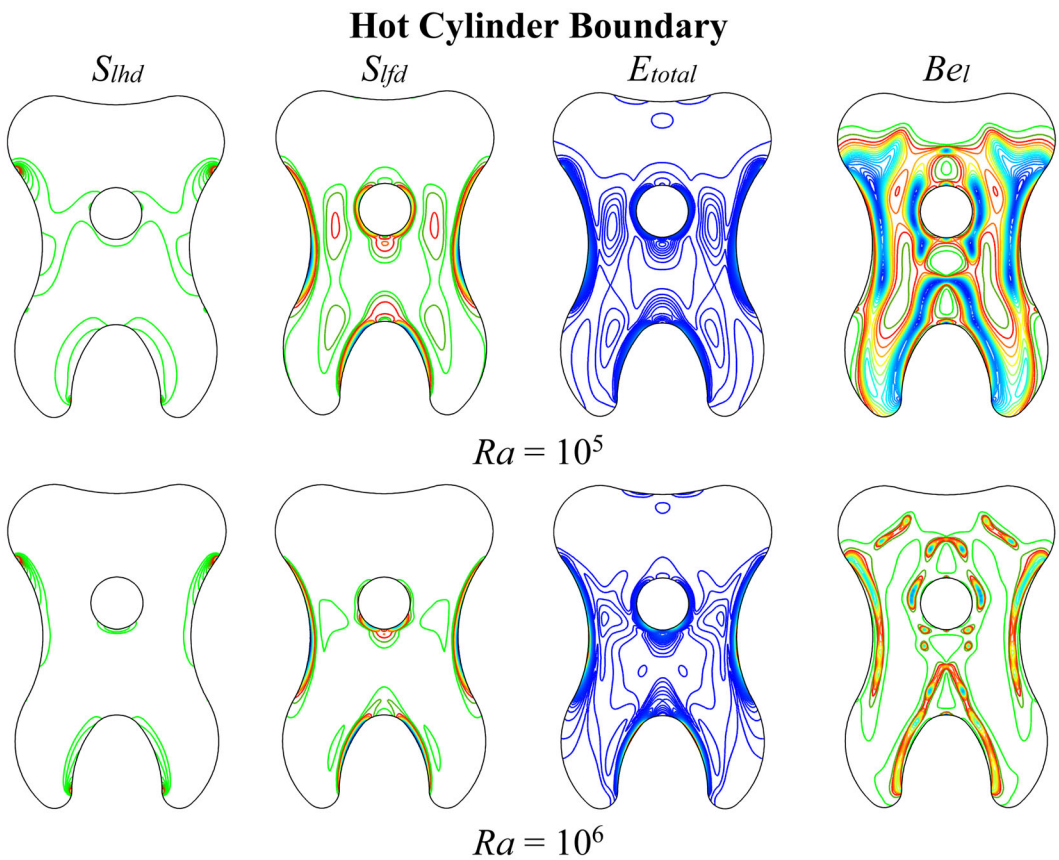


**FIGURE 10** Spatial distribution of various $E_{gen}$ factors, including $S_{lhd}$, $S_{lfd}$, $E_{total}$, and $Be_l$ for $Ra = 10^5$ and $Ra = 10^6$ at $\varphi = 10^{-4}$ under hot cylinder boundary conditions.

that the smoother flow near the walls generates increased fluid friction, which serves as a significant source of $E_{gen}$. Moreover, the cold walls, lower heated walls, and heated cylinder walls feature higher values in the local *Be* contours. This suggests that the regions with elevated *Be* values near the walls experience more efficient HT. Additionally, the presence of the heated cylinder changes the flow direction patterns, creating zones of recirculation. This enhances fluid mixing and boosts HT through convective processes.

## 5.5 | Variability in entropy generation (Case 4)

In the scenario where a cold cylinder boundary condition is present, at elevated *Ra* values, convective effects become more prominent, influencing the fluid movements and contributing to the level of entropy generation primarily in the lower portion of the tooth-shaped geometry.

As illustrated in Figure 11, raising the *Ra* value leads to a substantial enhancement of the contour along the left and right cold walls, as well as the lower wall. When $E_{gen}$ due to HT being dominant, it can be observed that with an increasing value of *Ra*, contours are nonuniform, leading to a high variation of temperature in the lower section. Conversely, elevating the *Ra* value leads to the emergence of additional vortices near the bottom wall and the cylinder wall, particularly when

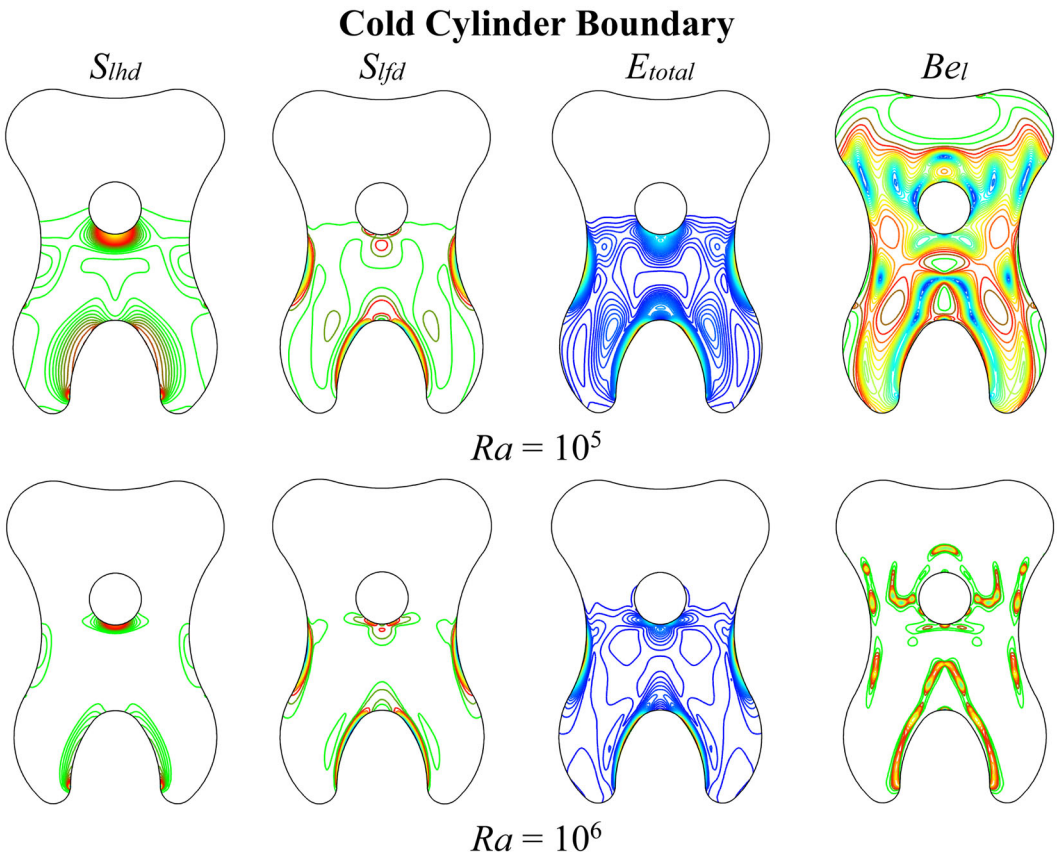


FIGURE 11 Spatial distribution of various $E_{gen}$ factors, including $S_{lhd}$, $S_{lfd}$, $E_{total}$, and $Be_l$ for $Ra = 10^5$ and $Ra = 10^6$ at $\varphi = 10^{-4}$ under cold cylinder geometry.

viscous dissipation exerts significant influence within the lower portion of the geometry. This phenomenon subsequently contributes to an increase in HT rate along both the bottom wall and the cylinder wall. Likewise, in comparison to the heated cylinder boundary conditions, the average $E_{gen}$ decreases as a result of greater HT along the lower wall and the influence of a cold cylinder wall. However, in the case of *Be*, as HT decreases, *Ra* increases, resulting in nonuniform contours near the cylinder wall. Consequently, the contour towards the cylinder wall diminishes due to the prevalence of HT effects. Meanwhile, the average value of *Be* rises, leading to an inefficient geometric model when compared to conditions involving a heated cylinder boundary.

**TABLE 3** Variation of $Nu_{avg}$, $E_{avg}$, and *Be* of hot cylinder and cold cylinder boundaries.

| Hot Cylinder Boundary | | | | Cold Cylinder Boundary | | | |
|---|---|---|---|---|---|---|---|
| ***Ra*** | $Nu_{avg}$ | $E_{avg}$ | ***Be*** | ***Ra*** | $Nu_{avg}$ | $E_{avg}$ | ***Be*** |
| $10^3$ | 5.61 | 5.80 | 1.01 | $10^3$ | 2.55 | 2.58 | 0.99 |
| $10^4$ | 5.69 | 6.20 | 0.896 | $10^4$ | 2.585 | 2.69 | 0.90 |
| $10^5$ | 8.13 | 33.08 | 0.27 | $10^5$ | 5.24 | 21.99 | 0.285 |
| $10^6$ | 15.388 | 641.48 | 0.041 | $10^6$ | 10.85 | 450.29 | 0.032 |

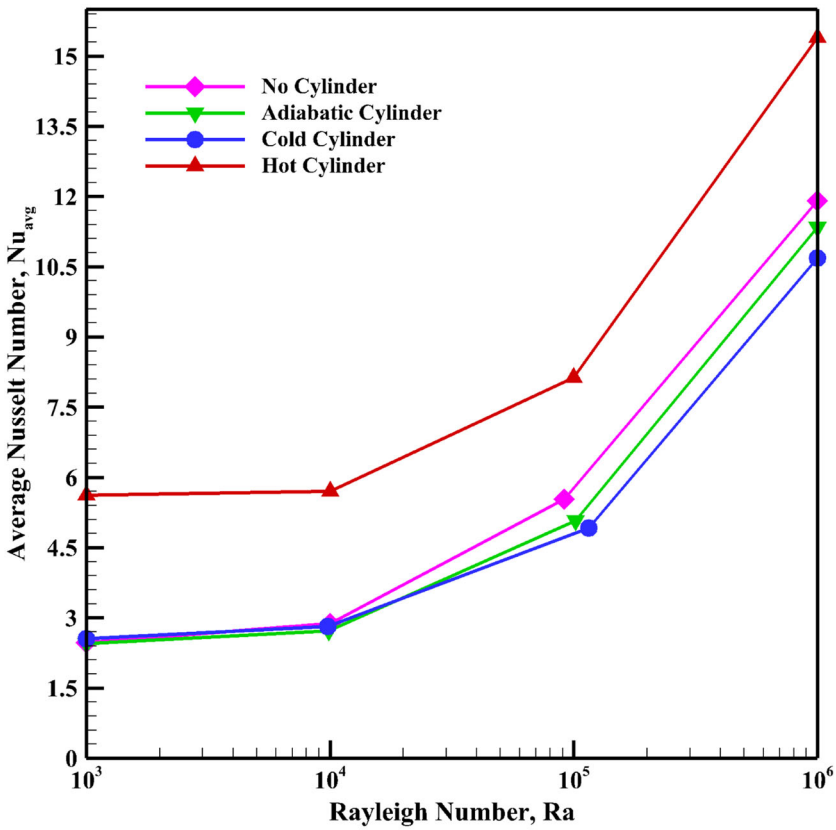


**FIGURE 12** *Ra* versus $Nu_{avg}$ variation with varying cylinder boundary conditions.

Table 3 illustrates that under both cold cylinder and hot cylinder boundary conditions, there is an observed increase in $Nu_{avg}$ and a decrease in *Be* as *Ra* values increase. This outcome is as anticipated, given that higher *Ra* values signify larger temperature differentials between the wall and the fluid. Consequently, this leads to increase HT rates. The results also reveal that with an increase in the *Ra* value from $10^3$ to $10^6$, the average $E_{gen}$ rises consistently for both conditions, as previously mentioned. Additionally, it becomes evident that employing a cylinder within the tooth-shaped cavity results in a lower average $E_{gen}$ under the same heating conditions. Notably, the data demonstrates a trend of lower average $E_{gen}$ at lower *Ra* values, and conversely, a higher average $E_{gen}$ at higher *Ra* values. Turning to the *Be* values, it is noticeable that for both conditions at $Ra = 10^3$, the *Be* value exceeds 0.5. This observation suggests that $E_{gen}$, attributed to the temperature gradient, holds greater influence compared to $E_{gen}$ resulting from fluid friction. On the contrary, with *Ra* values ranging from $10^4$ to $10^6$, *Be* values decrease below 0.5, indicating that $E_{gen}$, attributed to viscous resistance, becomes more significant compared to $E_{gen}$ resulting from the temperature gradient. In the scenario of a cold cylinder boundary condition, the $Nu_{avg}$ value exhibits an increase from 2.55 to 10.85, accompanied by a rise in the value of $E_{avg}$ from 2.58 to 450.29, while the value of *Be* decreases from 0.99 to 0.032. These shifts correspond to the escalation of *Ra* values from $10^3$ to $10^6$. Similarly, under the conditions of a hot cylinder, the $Nu_{avg}$ value undergoes an increment from 5.61 to 15.39, with the $E_{avg}$ value ascending from 5.80 to 641.48, and the *Be* value decreasing from 1.01 to 0.041, again as *Ra* values

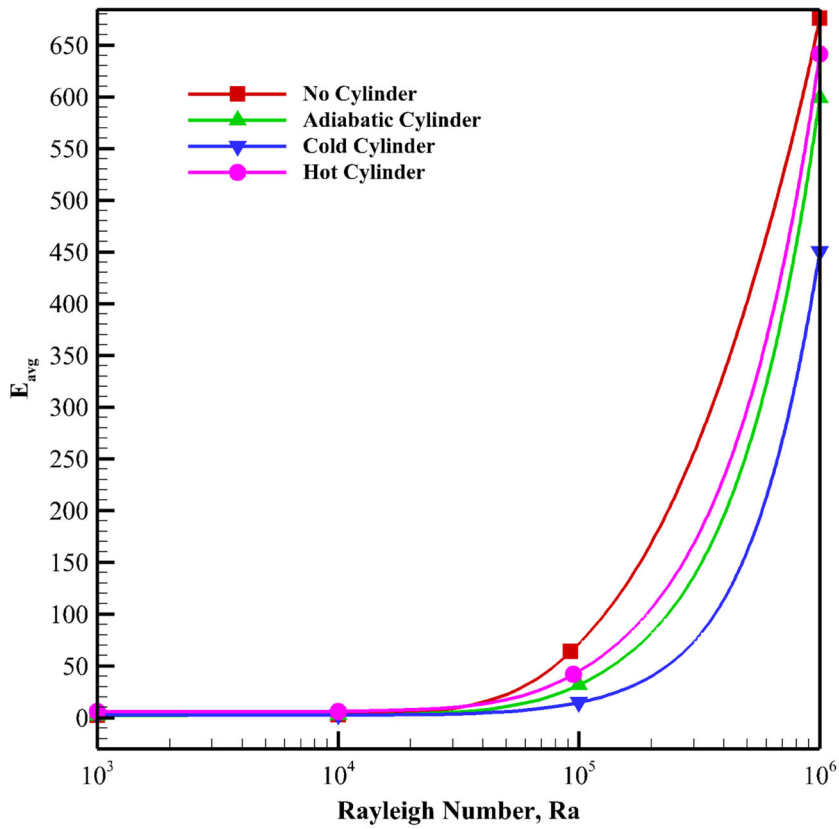


FIGURE 13 *Ra* versus Average $E_{gen}$ variation with varying cylinder boundary conditions.

ascend from $10^3$ to $10^6$. Upon comparing the outcomes for the cold cylinder and the hot cylinder in Table 3, it becomes evident that $Nu_{avg}$ generally exhibits higher values for the hot cylinder configuration. This observation implies that HT is more efficient in the case of a hot cylinder setup.

Figure 12 presents a comparison between $Ra$ and $Nu_{avg}$ for all four boundary conditions. Notably, the graph highlights that the hot cylinder's performance stands out at the top, whereas the cold cylinder boundary condition yields comparatively poorer results across all four-cylinder boundary conditions. Additionally, a clear trend emerges: with an increase in $Ra$, there is a corresponding increase in $Nu_{avg}$. Upon careful analysis of the data in Figure 12, it becomes evident that $Nu_{avg}$ consistently exhibits higher values for the hot cylinder condition compared to the other boundary conditions for the cylinders. This disparity suggests that HT is notably more effective in the case of the hot cylinder boundary condition.

The concept of average $E_{gen}$ serves as a crucial analytical tool in the study of tooth-shaped cavity flow modeling. In this context, Figure 13 provides an illustrative comparison between $Ra$ and the average $E_{gen}$ across four distinct cylinder boundary conditions. This visualization sheds light on the intricate relationship between these parameters in the context of the system under investigation. A noteworthy observation from the graph is that the scenario without a cylinder yields the highest average $E_{gen}$ when contrasted with the other cylinder boundary conditions. Interestingly, the cold cylinder boundary condition is associated with the least $E_{gen}$, indicating a more efficient outcome.

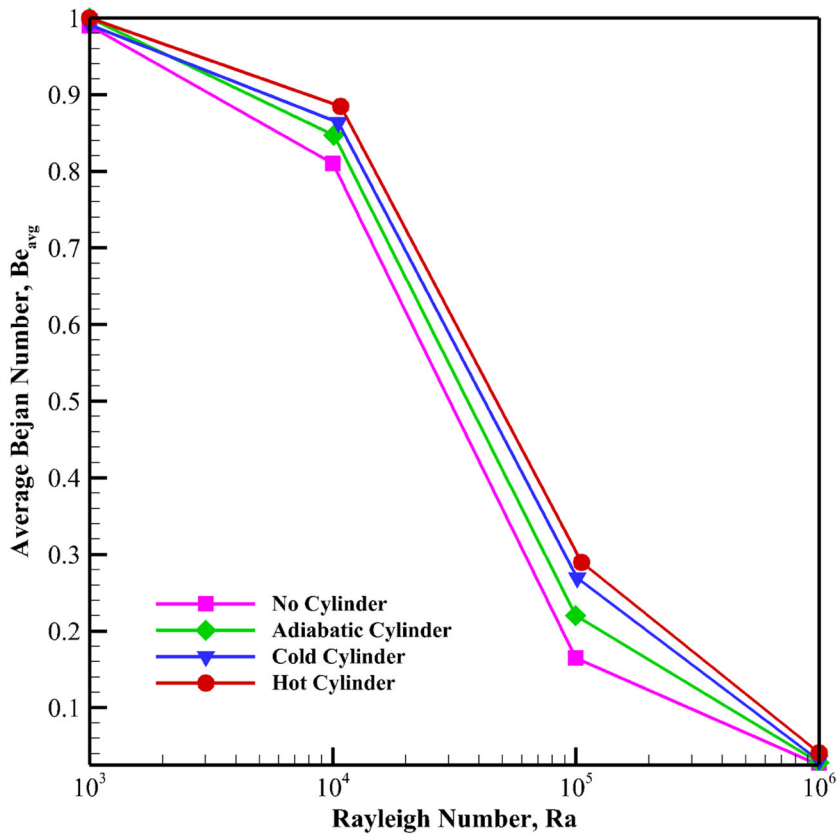


FIGURE 14 *Ra* versus average *Be* variation with varying cylinder boundary conditions.

Moreover, the hot cylinder and adiabatic cylinder conditions also exhibit relatively lower $E_{gen}$ compared to the scenario without a cylinder. As *Ra* increases, there is a corresponding rise on average *Egen*. This suggests that higher *Ra* values are associated with decreased overall system efficiency. Notably, the cold cylinder boundary condition proves to be particularly effective in this context, as its ability to generate less entropy significantly enhances the system's effectiveness. Furthermore, the hot and adiabatic cylinder conditions also exhibit improved efficiency when compared to scenarios with no cylinder boundary conditions.

However, in the context of cavity flow analysis, an increase in *Be* indicates that HT rate becomes more prominent than the rate of energy destruction. Figure 14 illustrates the relationship between *Ra* and the average *Be*. It is evident from the graph that raising *Ra* corresponds to a reduction in the average *Be*. Furthermore, the graph reveals a distinct trend among different cylinder boundary conditions. Specifically, it highlights that *Be* association with the hot cylinder boundary condition is notably higher than that of other boundary conditions. This observation suggests that in scenarios involving a hot cylinder boundary, HT takes center stage. This emphasis on HT leads to significant improvements in HT efficiency, resulting in a notably more energy-efficient system.

Moreover, in cavity flow analysis, the ecological coefficient performance (ECOP) aspect remains a significant factor. When observing Figure 15, it becomes apparent that changes in ECOP values are influenced by different *Ra* and various cylinder boundary conditions. The

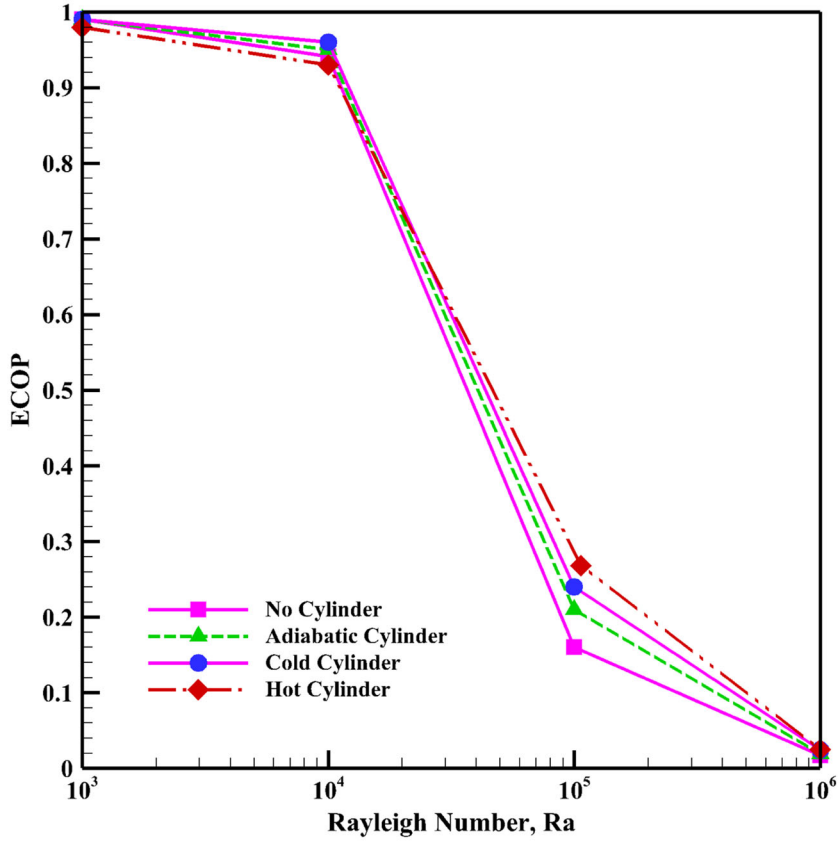


FIGURE 15 Comparison of *Ra* versus ECOP for various cylinder boundary conditions.

findings reveal an interesting trend: as *Ra* increases, the ECOP value actually decreases. Notably, the analysis indicates that the highest ECOP values are attained with the hot cylinder boundary conditions, whereas the no-cylinder boundary cases exhibit lower values compared to other boundary conditions. A higher ECOP value suggests improved system efficiency, which consequently leads to a reduced environmental impact. This observation highlights the effectiveness of the hot cylinder boundary configuration in the context of tooth-shaped cavity flow, showcasing its potential to offer superior environmental performance.

## 6 | CONCLUSIONS

A computational simulation of two-dimensional laminar NC fluid flow and HT within a tooth-shaped cavity has been conducted, employing various boundary conditions for a circular cylinder. The effects of varying *Ra* on HT and flow inside the cavity are investigated through visualizations and $Nu_{avg}$ calculations. Notably, the availability of the cylinder inside the cavity markedly affects the HT characteristics and $E_{gen}$ of the system. The work's primary conclusions are as follows:

- Buoyancy forces exert a significant influence on both flow patterns and HT characteristics within the cavity, a phenomenon observed consistently across all investigated *Ra* values.
- The implementation of an adiabatic cylinder leads to a slight decrease in the rate of HT when compared to the arrangement where the cylinder is not present.
- Hot cylinder boundary conditions facilitate the process of fluid mixing and result in the enhancement of HT, thereby increasing the efficiency of the system. On the other hand, when the boundary conditions are set to cold cylinder conditions, it negatively impacts the heat transfer process, leading to poor HT performance and decreased efficiency.
- The mean $E_{gen}$ rises with increasing *Ra* values, especially at higher *Ra* values, whereas the average *Be* decreases and attains its minimum at higher *Ra* values.

In general, the presence of a heated cylinder inside a tooth-shaped cavity significantly affects HT characteristics of the system, increasing HT and consequently, this leads to an improvement in the overall thermal efficiency of the system. Moreover, $Nu_{avg}$ increases significantly due to its characteristic length scale and higher HT throughout the domain. Furthermore, the forthcoming inquiry will encompass an investigation into the variation in the size and shape of the circular cylinder. The effects of a rotating cylinder were not addressed in the study, presenting a potential avenue for future research. The introduction of nanofluids and hybrid nanofluids was not undertaken in this study, offering another promising area for exploration in future research. Numerical uncertainty analysis, a critical addition to future research endeavors, was not covered in the current study.

## NOMENCLATURE

| | |
|---|---|
| $Be$ | Bejan number |
| $Be_l$ | local Bejan number |
| $E_{\text{avg}}$ | average entropy generation |
| $E_{\text{gen}}$ | entropy generation |
| $E_{total}$ | total entropy generation |
| $k$ | thermal conductivity (W/m.K) |

$L$ length (m)
$Nu$ Nusselt number
$Nu_{avg}$ average Nusselt number
$Pr$ Prandtl number
$Ra$ Rayleigh number
$S$ dimensionless entropy generation
$S_{lhd}$ entropy generation due to temperature gradient
$S_{lfd}$ entropy generation due to viscous dissipation
$T$ temperature (K)
$T_o$ bulk temperature $(T_h + T_c/2)$ (K)
$u, v$ velocity components in $x$ and $y$ directions (m/s)
$U, V$ dimensionless velocity components
$x, y$ dimensional Cartesian coordinates (m)
$X, Y$ dimensionless Cartesian coordinates
$\psi$ nondimensional stream function
$\Omega$ nondimensional vorticity

## GREEK SYMBOLS

$\alpha$ thermal diffusivity ($m^2/s$)
$\beta$ thermal expansion coefficient ($k^{-1}$)
$\varphi$ irreversibility factor
$\nu$ kinematic viscosity ($m^2/s$)
$\theta$ dimensionless temperature
$\mu$ viscosity ($Ns/m^{-2}$)
$\rho$ density ($kg/m^3$)
$g$ gravitational acceleration ($ms^{-2}$)

## SUBSCRIPTS

*avg* average
*c* cold
*f* base Fluid
*h* hot
*l* local
*t* total

## ACKNOWLEDGMENTS

Open access publishing facilitated by University of Technology Sydney, as part of the Wiley - University of Technology Sydney agreement via the Council of Australian University Librarians.

## CONFLICTS OF INTEREST STATEMENT

The authors declare no conflict of interest.

## DATA AVAILABILITY STATEMENT

All data are available in the manuscript.

## ORCID

*Jahidul Islam Jihan* http://orcid.org/0009-0007-4369-9148
*Md. Zobaer Ahammad* http://orcid.org/0009-0006-2553-4991
*Suvash C. Saha* http://orcid.org/0000-0002-9962-8919

## REFERENCES

1. Mebarek-Oudina F, Fares R, Aissa A, Lewis RW, Abu-Hamdeh N. H. Entropy and convection effect on magnetized hybrid nano-liquid flow inside a trapezoidal cavity with zigzagged wall. *Int Commun Heat Mass Transfer*. 2021;125:105279. doi:10.1016/j.icheatmasstransfer.2021.105279
2. Oliveski RDC, Macagnan MH, Copetti JB. Entropy generation and natural convection in rectangular cavities. *Appl Therm Eng*. 2009;29(8):1417-1425. doi:10.1016/j.applthermaleng.2008.07.012
3. Yilbas BS, Shuja SZ, Gbadebo SA, Al-Hamayel HIA, Boran K. Natural convection and entropy generation in a square cavity. *Int J Energy Res*. 1998;22(14):1275-1290. doi:10.1002/(SICI)1099-114X(199811)22:14<1275::AID-ER453>3.0.CO;2-B
4. Chandra Roy N, Monira S, Subba Reddy Gorla R. Buoyancy-driven flow of magnetohydrodynamic hybrid nanofluids in an open cavity with permeable horizontal walls. *Proc Institut Mech Eng N: J Nanomater Nanoeng Nanosyst*. 2023. doi:10.1177/23977914231151481
5. Momoniat E, Harley C, Herbst RS. Effects of extended surfaces on heat transfer in buoyancy-driven flow in a square cavity. *Results Eng*. 2023;18:101190. doi:10.1016/j.rineng.2023.101190
6. Akhter R, Mokaddes Ali M, Alim MA. Entropy generation due to hydromagnetic buoyancy-driven hybrid-nanofluid flow in partially heated porous cavity containing heat conductive obstacle. *Alex Eng J*. 2023;62:17-45. doi:10.1016/j.aej.2022.07.005
7. Kuyper RA, Van Der Meer TH, Hoogendoorn CJ, Henkes RAWM. Numerical study of laminar and turbulent natural convection in an inclined square cavity. *Int J Heat Mass Transfer*. 1993;36(11):2899-2911. doi:10.1016/0017-9310(93)90109-J
8. Kumar A, Sinha MK. Buoyancy driven flow through a square enclosure. *Mater Today: Proc*. 2022;56:2780-2784. doi:10.1016/j.matpr.2021.10.091
9. Mobedi M. Conjugate natural convection in a square cavity with finite thickness horizontal walls. *Int Commun Heat Mass Transfer*. 2008;35(4):503-513. doi:10.1016/j.icheatmasstransfer.2007.09.004
10. Rejeesh ADA, Udhayakumar S, Sekhar TVS, Sivakumar R. Mixed convection and heat transfer studies in non-uniformly heated buoyancy driven cavity flow. *Open J Fluid Dynam*. 2017;07(2):231-262. doi:10.4236/ojfd.2017.72016
11. Chaabane R, Kolsi L, Jemni A, D'Orazio A. Buoyancy driven flow characteristics inside a cavity equiped with diamond elliptic array. *Int J Nonlin Sci Num Simulat*. 2022;24(6):2163-2177. doi:10.1515/ijnsns-2021-0073
12. Hatami M. Numerical study of nanofluids natural convection in a rectangular cavity including heated fins. *J Mol Liq*. 2017;233:1-8. doi:10.1016/j.molliq.2017.02.112
13. Yousaf M, Usman S. Natural convection heat transfer in a square cavity with sinusoidal roughness elements. *Int J Heat Mass Transfer*. 2015;90:180-190. doi:10.1016/j.ijheatmasstransfer.2015.06.049
14. Sheremet M, Pop I, Öztop HF, Abu-Hamdeh N. Natural convection of nanofluid inside a wavy cavity with a non-uniform heating: entropy generation analysis. *Int J Num Methods Heat Fluid Flow*. 2017;27(4):958-980. doi:10.1108/HFF-02-2016-0063
15. Saha T, Islam T, Yeasmin S, Parveen N. Thermal influence of heated fin on MHD natural convection flow of nanofluids inside a wavy square cavity. *Int J Thermofluids*. 2023;18:100338. doi:10.1016/j.ijft.2023.100338
16. Siavashi M, Yousofvand R, Rezanejad S. Nanofluid and porous fins effect on natural convection and entropy generation of flow inside a cavity. *Adv Powder Technol*. 2018;29(1):142-156. doi:10.1016/j.apt.2017.10.021
17. Basak T, Roy S, Balakrishnan AR. Effects of thermal boundary conditions on natural convection flows within a square cavity. *Int J Heat Mass Transfer*. 2006;49(23):4525-4535. doi:10.1016/j.ijheatmasstransfer.2006.05.015
18. Sen N, Nag S, Bamboowala HT, Manna NK, Biswas N, Mandal DK. Magnetohydrodynamic thermal behavior of nanofluid flow in a trapezoidal cavity subjected to non-uniform heating. *Mater Today: Proc*. 2022;63:320-327. doi:10.1016/j.matpr.2022.03.144

19. Biswas N, Manna NK, Mahapatra PS. Merit of non-uniform over uniform heating in a porous cavity. *Int Commun Heat Mass Transfer*. 2016;78:135-144. doi:10.1016/j.icheatmasstransfer.2016.09.001
20. Mullick SH, Kumar A, Kundu PK. Numerical study of natural convection inside a square cavity with non-uniform heating from top. *J Instit Eng C*. 2020;101(6):1043-1050. doi:10.1007/s40032-020-00618-y
21. Natarajan E, Basak T, Roy S. Natural convection flows in a trapezoidal enclosure with uniform and non-uniform heating of bottom wall. *Int J Heat Mass Transfer*. 2008;51(3):747-756. doi:10.1016/j.ijheatmasstransfer.2007.04.027
22. Aljabair S, Ekaid AL, Ibrahim SH, Alesbe I. Mixed convection in sinusoidal lid driven cavity with non-uniform temperature distribution on the wall utilizing nanofluid. *Heliyon*. 2021;7(5):e06907. doi:10.1016/j.heliyon.2021.e06907
23. Khanafer K, Aithal SM, Vafai K. Mixed convection heat transfer in a differentially heated cavity with two rotating cylinders. *Int J Therm Sci*. 2019;135:117-132. doi:10.1016/j.ijthermalsci.2018.07.020
24. Şenel P. FHD flow in an irregular cavity subjected to a non-uniform magnetic field. *Commun Series A1 Math Statist*. 2023;72(2):530-550. doi:10.31801/cfsuasmas.1087827
25. Joe ES, Arumuga Perumal D. Computational analysis of nonhomogeneous fluid flow in a two-cylinder-driven rectangular cavity. *Appl Eng Sci*. 2021;7:100064. doi:10.1016/j.apples.2021.100064
26. Bilal S, Mahmood R, Majeed AH, Khan I, Nisar KS. Finite element method visualization about heat transfer analysis of newtonian material in triangular cavity with square cylinder. *J Mater Res Technol*. 2020;9(3):4904-4918. doi:10.1016/j.jmrt.2020.03.010
27. Mohammed AA, Mohammed AA, Channapattana S. Numerical study of convection air currents around a hot cylinder inside a triangular cavity. *Al-Nahrain J Eng Sci*. 2023;26(2):102-115. doi:10.29194/NJES.26020102
28. Moderres M, Benmalek T, Sofiane A, Ghezal A, Abboudi S, Benbrik A. Double-diffusive natural convection in a cavity with an inner cylinder wrapped by a porous layer. *Thermal Sci*. 2022;26(2):1841-1853. doi:10.2298/TSCI201112202M
29. Saleh H, Hashim I. Natural convection from a cylinder in square porous enclosure filled with nanofluids. *J Porous Media*. 2015;18(6):559-567. doi:10.1615/JPorMedia.v18.i6.10
30. Tayebi T, Chamkha AJ. Entropy generation analysis due to MHD natural convection flow in a cavity occupied with hybrid nanofluid and equipped with a conducting hollow cylinder. *J Therm Anal Calorim*. 2020;139(3):2165-2179. doi:10.1007/s10973-019-08651-5
31. Roslan R, Saleh H, Hashim I, Bataineh AS. Natural convection in an enclosure containing a sinusoidally heated cylindrical source. *Int J Heat Mass Transfer*. 2014;70:119-127. doi:10.1016/j.ijheatmasstransfer.2013.10.011
32. Tayebi T, Chamkha AJ. Magnetohydrodynamic natural convection heat transfer of hybrid nanofluid in a square enclosure in the presence of a wavy circular conductive cylinder. *J Therm Sci Eng Appl*. 2020;12(3):Article 4044857. doi:10.1115/1.4044857
33. Alsabery AI, Tayebi T, Roslan R, Chamkha AJ, Hashim I. Entropy generation and mixed convection flow inside a wavy-walled enclosure containing a rotating solid cylinder and a heat source. *Entropy*. 2020;22(6):606. doi:10.3390/E22060606
34. Alsabery A, Tayebi T, Chamkha A, Hashim I. Effects of non-homogeneous nanofluid model on natural convection in a square cavity in the presence of conducting solid block and corner heater. *Energies*. 2018;11(10):2507. doi:10.3390/en11102507
35. Alhashash A. Free convection heat transfer in composite enclosures with porous and nanofluid layers. *Adv Math Phys*. 2023;2023:1-16. doi:10.1155/2023/8426825
36. Dogonchi AS, Sadeghi MS, Ghodrat M, Chamkha AJ, Elmasry Y, Alsulami R. Natural convection and entropy generation of a nanoliquid in a crown wavy cavity: effect of thermo-physical parameters and cavity shape. *Case Stud Thermal Eng*. 2021;27:101208. doi:10.1016/j.csite.2021.101208
37. Saboj JH, Nag P, Saha G, Saha SC. Entropy production analysis in an octagonal cavity with an inner cold cylinder: a thermodynamic aspect. *Energies*. 2023;16(14):5487. doi:10.3390/en16145487
38. Saleh H, Siri Z, Hashim I. Role of fluid-structure interaction in mixed convection from a circular cylinder in a square enclosure with double flexible oscillating fins. *Int J Mech Sci*. 2019;161–162:105080. doi:10.1016/j.ijmecsci.2019.105080

39. Saha G, Al-Waaly AAY, Paul MC, Saha SC. Heat transfer in cavities: configurative systematic review. *Energies*. 2023;16(5):2338. doi:10.3390/en16052338
40. Ikram MM, Saha G, Saha SC. Conjugate forced convection transient flow and heat transfer analysis in a hexagonal, partitioned, air filled cavity with dynamic modulator. *Int J Heat Mass Transfer*. 2021;167:120786. doi:10.1016/j.ijheatmasstransfer.2020.120786
41. Ikram MM, Saha G, Saha SC. Unsteady conjugate heat transfer characteristics in hexagonal cavity equipped with a multi-blade dynamic modulator. *Int J Heat Mass Transfer*. 2023;200:123527. doi:10.1016/j.ijheatmasstransfer.2022.123527
42. Ikram MM, Saha G, Saha SC. Second law analysis of a transient hexagonal cavity with a rotating modulator. *Int J Heat Mass Transfer*. 2024;221:125039. doi:10.1016/j.ijheatmasstransfer.2023.125039
43. Zidan AM, Tayebi T, Sattar Dogonchi A, Chamkha AJ, Ben Hamida MB, Galal AM. Entropy-based analysis and economic scrutiny of magneto thermal natural convection enhancement in a nanofluid-filled porous trapezium-shaped cavity having localized baffles. *Waves Random Complex Media*. 2022. doi:10.1080/17455030.2022.2084651
44. Tirth V, Pasha AA, Tayebi T, et al. Magneto double-diffusive free convection inside a C-shaped nanofluid-filled enclosure including heat and solutal source block. *Case Stud Thermal Eng*. 2023;45:102942. doi:10.1016/j.csite.2023.102942
45. Tayebi T, Dahmane F, Jamshed W, Chamkha AJ, El Din SM, Raizah Z. Double-diffusive magneto-natural convection of nanofluid in an enclosure equipped with a wavy porous cylinder in the local thermal non-equilibrium situation. *Case Stud Thermal Eng*. 2023;43:102785. doi:10.1016/j.csite.2023.102785
46. Biswas N, Manna NK, Datta A, Mandal DK, Benim AC. Role of aspiration to enhance MHD convection in protruded heater cavity. *Progress Computat Fluid Dynam Int J*. 2020;20(6):363-378. doi:10.1504/PCFD.2020.111408
47. Biswas N, Manna NK. Enhanced convective heat transfer in lid-driven porous cavity with aspiration. *Int J Heat Mass Transfer*. 2017;114:430-452. doi:10.1016/j.ijheatmasstransfer.2017.06.078
48. Vishnu AS, Aravind GP, Deepu M, Sadanandan R. Effect of heat transfer on an angled cavity placed in supersonic flow. *Int J Heat Mass Transfer*. 2019;141:1140-1151. doi:10.1016/j.ijheatmasstransfer.2019.07.058
49. Khanafer K, Vafai K. Effect of a circular cylinder and flexible wall on natural convective heat transfer characteristics in a cavity filled with a porous medium. *Appl Therm Eng*. 2020;181:115989. doi:10.1016/j.applthermaleng.2020.115989
50. Ilis GG, Mobedi M, Sunden B. Effect of aspect ratio on entropy generation in a rectangular cavity with differentially heated vertical walls. *Int Commun Heat Mass Transfer*. 2008;35(6):696-703. doi:10.1016/j.icheatmasstransfer.2008.02.002
51. Bagai S, Kumar M, Patel A. Mixed convection in four-sided lid-driven sinusoidally heated porous cavity using stream function-vorticity formulation. *SN Appl Sci*. 2020;2(12):2066. doi:10.1007/s42452-020-03815-7
52. Singh AK, Roy S, Basak T. Analysis of entropy generation due to natural convection in tilted square cavities. *Ind Eng Chem Res*. 2012;51(40):13300-13318. doi:10.1021/ie3013665
53. Magherbi M, Abbassi H, Ben Brahim A. Entropy generation at the onset of natural convection. *Int J Heat Mass Transfer*. 2003;46(18):3441-3450. doi:10.1016/S0017-9310(03)00133-9
54. Ahlawat A, Sharma MK. Effects of heated block comprised porous stratum and micropolar hybrid nanofluid on convective heat transfer and entropy generation in a square enclosure. *Heat Transfer*. 2022;51(6):5320-5347.
55. Saha G, Saha S, Hasan MN, Islam Md. Natural convection heat transfer within octagonal enclosure. *Int J Eng Trans A: Basics*. 2010;23(1):1-10.

**How to cite this article:** Saha BK, Jihan JI, Ahammad MZ, Saha G, Saha SC. Enhanced thermal performance and entropy generation analysis in a novel cavity design with circular cylinder. *Heat Transfer*. 2024;53:1446-1473. doi:10.1002/htj.22999